Single- and two-photon absorption induced all-optical control of gallium selenide integrated silicon nitride photonic devices in the 700–800 nm wavelength range

Asish Prosad ; Rabindra Biswas ; Lal Krishna A S ; T. Srinivas; Varun Raghunathan ✉

Check for updates

View Online

Export Citation

CrossMark

AIP Publishing

Single- and two-photon absorption induced all-optical control of gallium selenide integrated silicon nitride photonic devices in the 700–800 nm wavelength range

View Online   Export Citation   CrossMark

Asish Prosad, [ID] Rabindra Biswas, [ID] Lal Krishna A S, [ID] T. Srinivas, and Varun Raghunathan[a] [ID]

AFFILIATIONS

Department of Electrical Communication Engineering, Indian Institute of Science, Bangalore 560012, India

[a]Author to whom correspondence should be addressed: varunr@iisc.ac.in

ABSTRACT

In this work, we report single- and two-photon absorption (TPA) induced transmission and resonance modulation in a multilayer gallium selenide (GaSe) integrated silicon nitride (Si_3N_4) waveguide and ring resonator operating in the 700–800 nm wavelength range. Intensity dependent saturable absorption at low optical powers followed by TPA at higher power levels in GaSe integrated Si_3N_4 waveguides is observed at 785 nm pulsed laser excitation. A TPA coefficient of 0.117 cm/GW for the GaSe–Si_3N_4 composite waveguide and a three-photon absorption coefficient of 7.876×10^{-6} cm^3/GW^2 for the bare Si_3N_4 waveguide are extracted from intensity dependent transmission measurements. The single-photon absorption process induced by a blue laser incident on the multilayer GaSe transferred on top of the Si_3N_4 ring resonator is used for all-optical resonance tuning through the free-carrier refraction effect. A strong blue shift of the resonance by ~12.3 pm/mW combined with resonance broadening is observed due to the free-carrier induced refractive index and absorption modulation. The TPA in the GaSe integrated Si_3N_4 ring resonator is also shown to result in a blue shift of the resonances excited using a 785 nm pulsed laser. This work demonstrates the all-optical control of 2D material integrated Si_3N_4 guided-wave structures operating in the shorter near-infrared wavelength range with potential applications in integrated quantum photonics, miniaturized sensing devices, and biomedical imaging.

I. INTRODUCTION

Silicon nitride (Si_3N_4) on silicon dioxide (SiO_2) is considered as a promising material platform for realizing integrated photonic devices across a broad transparency window spanning visible to mid-infrared, with applications in chemical/biological sensing,[1] miniaturized medical probes,[2] quantum photonic circuits,[3] etc. Low-loss Si_3N_4 integrated optics leverages the mature silicon compatible fabrication processes, with demonstration of various high-quality passive devices, such as waveguides, interferometers, resonators, and photonic circuits.[4,5] The lack of light emission, detection, efficient modulation, and switching capabilities still limits the gamut of active optical functionalities that can be realized

using this platform.[6] Low-loss, long Si_3N_4 waveguides and high-quality factor resonant structures have been utilized to boost the inherent weak nonlinear optical properties of Si_3N_4 for realizing efficient nonlinear functionalities, such as supercontinuum generation,[7] wavelength conversion,[8] parametric amplification,[9] and frequency comb generation.[10] Thermo-optic modulation using Si_3N_4 guided-wave structures[11] and piezo-electric tuning of suspended Si_3N_4 waveguides[12] have also been demonstrated, albeit at low modulation speeds (few kHz to MHz). There is also interest in the heterogeneous integration of III–V gain media,[13] silicon photodetectors,[14] and lithium niobate based second-order nonlinear optical media[15] on Si_3N_4 guided-wave structures. Such heterogeneously integrated devices rely on precise wafer bonding to integrate the active medium

07 November 2023 04:27:21

on top of prefabricated Si_3N_4 photonic structures with careful consideration of the mismatch in mechanical and thermal properties of the two materials.

Another promising route to heterogeneous integration is the addition of two-dimensional (2D) layered materials on top of Si_3N_4 guided-wave structures for realizing active optical functionalities. Two-dimensional materials in metallic, semiconducting, or insulating form exhibit robust linear[16] and nonlinear optical properties,[17,18] making them promising candidates for realizing active photonic devices. 2D materials can be integrated onto photonic structures using simple dry transfer[19,20] or large area deposition[21,22] techniques. Enhanced Kerr effect, spectral broadening, and four-wave mixing (FWM) have been reported from 2D material integrated guided-wave structures, such as graphene oxide,[23–27] graphene,[28,29] molybdenum disulfide (MoS_2),[30–33] and tungsten disulfide (WS_2),[34] with underlying silicon and Si_3N_4 waveguides. An FWM conversion efficiency enhancement by 9.5 dB from a graphene oxide integrated Si_3N_4 waveguide[23] and 4 dB from a MoS_2 integrated silicon waveguide[33] and a fivefold increase in the Kerr coefficient from a gallium sulfide flake integrated Si_3N_4 micro-ring resonator[35] have been reported. Phase shifters and intensity modulators based on the integration of MoS_2 with Si_3N_4 micro-ring resonators have also been reported.[36] It is pointed out that most of the previous reports on 2D material integrated guided-wave structures are for end-applications in the telecommunication wavelength range. There is a clear and compelling need to extend such hybrid active photonics devices beyond the communication wavelength bands into visible, shorter near-infrared, and mid-infrared wavelengths.

With this motivation, we report single- and two-photon absorption (TPA) based all-optical control of transmission and resonance characteristics in a multilayer gallium selenide (GaSe) integrated Si_3N_4 waveguide and ring resonator operating in the shorter near-infrared wavelength range (700–800 nm). GaSe is a semiconducting monochalcogenide with an indirect bandgap of ~2 eV,[37] making it a promising material for realizing photonic devices across a wide transparency window. The ε-polytype of GaSe belonging to the D_{3h} point group exhibits strong layer independent second- and third-order optical nonlinearities.[38,39] In this paper, we first measure intensity dependent absorption processes in multilayer GaSe integrated Si_3N_4 waveguides using 785 nm pulsed laser excitation. We observe saturable absorption due to the filling of band-edge defect states at low optical intensity levels followed by two-photon absorption (TPA) due to two-photon induced band-to-band transition at higher optical intensities. A TPA coefficient of 0.117 cm/GW for the GaSe–Si_3N_4 composite waveguide and a three-photon absorption coefficient of 7.876×10^{-6} cm^3/GW^2 for the bare Si_3N_4 waveguide are extracted from intensity dependent transmission measurements. Single-photon absorption induced by a blue laser selectively incident on the GaSe flake on top of the Si_3N_4 ring resonator is used to demonstrate all-optical tuning of the resonances through the free-carrier refraction effect. The measured blue shift of the resonance of ~12.3 pm/mW and the associated resonance broadening are used to extract the free-carrier induced refractive index and absorption modulation. TPA in the GaSe integrated Si_3N_4 ring resonator is also used to demonstrate spectral tuning of resonances using 785 nm pulsed laser excitation. The experimental study in this work is aimed at demonstrating all-optical control of 2D material integrated Si_3N_4 photonic devices operating

in the shorter near-infrared wavelength with potential applications in sensing, biomedical imaging, and quantum photonics.

II. DEVICE FABRICATION AND 2D MATERIAL TRANSFER

The starting wafer for the fabrication of the Si_3N_4 waveguides is a silicon substrate with a 2 μm thick SiO_2 layer as the bottom cladding and a 350 nm Si_3N_4 waveguiding layer. The SiO_2 and Si_3N_4 layers are deposited using the low-pressure chemical vapor deposition (LPCVD) technique, with near stoichiometric Si:N composition. The starting sample is first cleaned in a piranha solution (3:1 of H_2SO_4:H_2O_2) followed by spin coating of hexamethyldisilazane (HMDS) for promoting adhesion. The waveguides and ring resonator structures are patterned using electron beam lithography (Raith e-LiNE) with a ma-N 2403 resist as the mask. The patterns are subsequently transferred onto a Si_3N_4 film using the plasma-assisted reactive ion etching (RIE) with oxygen and trifluoromethane (CHF_3) gas chemistry. Subsequently, grating couplers are written using e-beam lithography with alignment to the underlying layer and etched using RIE with a PMMA 950 A4 resist as the mask.

For transferring GaSe flakes on top of the fabricated waveguides and ring resonators, the multilayer GaSe (source material from 2D Semiconductors, Inc., USA) is first exfoliated using a polydimethylsiloxane (PDMS) sheet. Suitable flakes with a thickness of less than 20 nm are identified using a zoom lens setup through visual contrast. Using a dry transfer setup,[40] the flakes are carefully aligned to overlap with the waveguide or ring resonator and subsequently transferred by pressing the PDMS sheet onto the prefabricated structures.

III. EXPERIMENTAL STUDIES

A. Two-photon absorption measurements in GaSe integrated silicon nitride waveguides

The optical image of a Si_3N_4 waveguide of length 550 μm is shown in Fig. 1(a) after the transfer of GaSe flakes (indicated by the gray shaded contour). A zoomed-in view of the waveguide with the GaSe flakes is shown in Fig. 1(b) with two small flakes covering a total waveguide length of 35.2 μm with an ~8 μm separation. The flake thickness in Fig. 1(b) is measured to be ~16 nm using atomic force microscopy (AFM), which corresponds to ~18 to 19 layers. The cross-sectional scanning electron microscopy (SEM) image of the waveguide with the measured dimensions of 350×530 nm^2 and the top-view SEM image of the grating coupler are also shown in Figs. 1(c) and 1(d), respectively. The gratings are designed for optimum coupling of horizontally polarized light to the transverse electric (TE) mode of the waveguide. The measured dimensions of the grating are as follows: pitch = 487 nm, duty cycle = 50%, and etch depth = 180 nm. The grating of size 10×25 μm^2 gradually tapers to the intended waveguide width of 530 nm through an intermediate tapered section of 200 μm length.

Simulated mode profiles with and without the GaSe flake obtained using the Lumerical finite difference time-domain (FDTD)[41] are shown in the inset of Fig. 1(e). The GaSe flake is found to roll off along the side walls over a length of 150 nm as seen in the top-view SEM image shown in Fig. S1 of the supplementary material. The modal area before and after the addition of ~16 nm
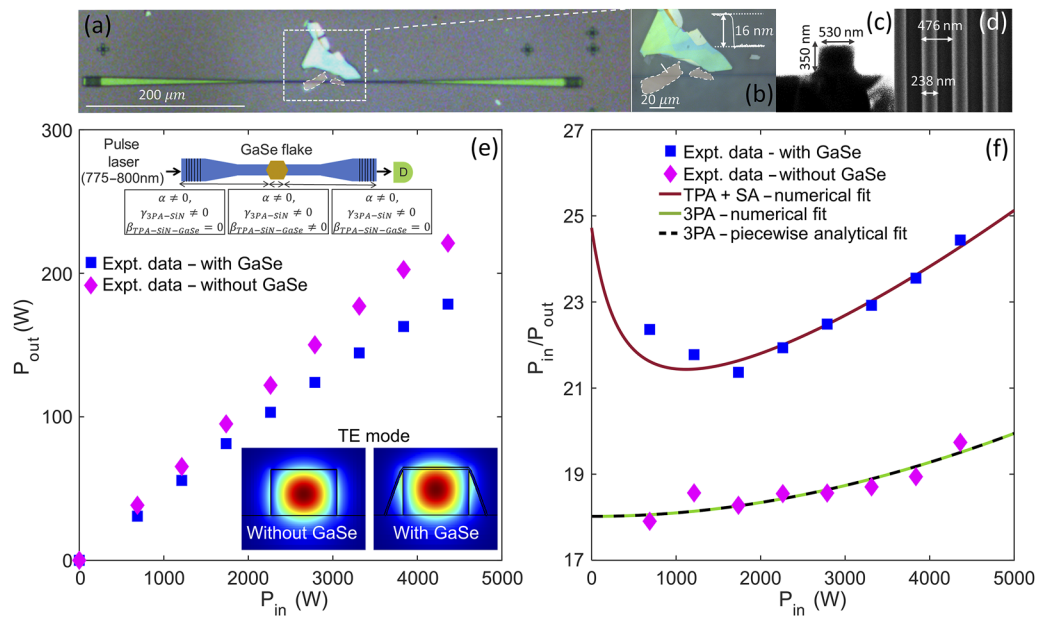
FIG. 1. (a) Optical image of the waveguide with multilayer GaSe transferred on top. (b) Zoomed-in view of the waveguide with the overlapping GaSe region highlighted. The AFM line scan of the GaSe flake corresponding to the region marked by arrow is also shown. (c) Cross section SEM image of the waveguide. (d) Top-view SEM image of the grating coupler with the dimensions indicated. (e) Measured peak power at the output of the waveguide as a function of input peak power, with and without the GaSe flake. A schematic of the waveguide and GaSe flake with the linear, two-photon, and three-photon absorption coefficients considered in each segment is shown as an inset. The simulated TE-mode field profiles of the waveguide with and without GaSe are shown as an inset (f) Ratio of the input to output power as a function of input peak power. The optical power measured at the input fiber tip and output fiber tip are considered here to calculate the peak power.

thick GaSe flake is calculated to be 0.086 and 0.095 μm^2, respectively. Introducing the multilayer GaSe results in a slight increase in the mode field distribution as the optical mode overlaps with the higher refractive index of the GaSe layer (n ~ 2.8). The corresponding field overlap with the GaSe layer is calculated to be ~2.32%. The Raman spectrum from the multilayer GaSe flake transferred onto the Si_3N_4 photonic structure is shown in Fig. S2 of the supplementary material.

The orientation of the flake with reference to the waveguide is determined using the polarization dependent second-harmonic generation (SHG) and third-harmonic generation (THG) measurements on the GaSe flake on top of the waveguide. This is shown in Fig. S3 of the supplementary material. The SHG polar plot shows a characteristic sixfold symmetry as expected for GaSe with a hexagonal lattice with the orientation of its armchair axis at 50° to the waveguide long axis. The angular offset between the 2D material and waveguide does not affect the third-order nonlinear optical process as seen from the polarization independence of the THG response. The same polarization independence is expected for the two-photon absorption process as well due to its third-order nonlinear optical origin.

Loss measurements performed on the straight waveguides in the absence of the 2D material using the cut-back method with low-power continuous-wave excitation (785 nm center wavelength and 5.6 mW power) resulted in propagation and coupling losses of 3.5 dB/cm and 3.8 dB per coupler section, respectively. These data are shown in Fig. S4 of the supplementary material. In the presence

of the GaSe flake on top of the waveguide, the overall insertion loss increased by 1.2 dB. The excess loss measurements were performed for only one GaSe flake transferred onto the Si_3N_4 waveguide due to the difficulty in obtaining multiple such samples of distinct length, similar thickness, and flake adhesion. This prevented the separation of the excess loss into coupling and propagation losses.

For optical power dependent transmission measurements, a pulsed laser source (frequency doubled OPO, APE GmbH) with 100 fs pulse width, 80 MHz repetition rate, and 785 nm center wavelength is coupled into the waveguide using the grating coupler. The input power coupled into the waveguide is varied, and the average out-coupled power is measured using a powermeter (Thorlabs, S120C). This measurement is repeated for the same waveguide before and after the transfer of the multilayer GaSe flake. The coupling losses under low-power pulsed excitation are found to increase by an additional 2.3 dB per coupler, which can be attributed to small perturbations to the fiber tip under pulsed excitation and wavelength response of the grating coupler. The optical spectra at the input and output of the waveguide both in the absence and in the presence of the GaSe flake for three different average power levels are shown in Fig. S5 of the supplementary material. A slight reduction in the spectral widths is observed at the output of the waveguide for low incident powers. This is mainly attributed to the offset in the grating coupler transmission relative to the input excitation spectrum and spectral modulations due to the self-phase modulation effect. With increasing incident power, the spectral width increases at the output of the waveguide closely following the input spectral characteris-

tics. This points to the grating coupler not significantly altering the light coupling. Negligible spectral broadening observed at the output of the Si$_3$N$_4$ waveguides can be ascribed to the short length of the waveguide considered here, their normal dispersion properties (refer to Fig. S6 of the supplementary material), and the inherently weak Kerr optical nonlinearity. The spectra are found to be unaltered in the presence of the GaSe flake. The top-view optical image of the waveguide with the coupled light propagating along the waveguide is shown in Fig. S7 of the supplementary material.

Figure 1(e) shows the variation in the out-coupled peak optical power as a function of input peak optical power measured at the output and input fiber tips, respectively. The out-coupled power is found to noticeably saturate in the presence of the GaSe layer in comparison with the waveguide without the GaSe layer. The saturation of transmission in the presence of the 2D material is attributed to enhanced multiphoton absorption, in particular, two-photon absorption.[42,43] Figure 1(f) shows the ratio of the input to output power, $R = \frac{P_{in}}{P_{out}}$, as a function of varying input peak optical power (P_{in}). For the case of the Si$_3$N$_4$ waveguide without the GaSe flake, the power ratio shows a slight super-linear increase with increasing input power. This increase in the power ratio is attributed to three-photon absorption (3PA) occurring in the Si$_3$N$_4$ waveguide. The large bandgap observed for stoichiometric LPCVD Si$_3$N$_4$ (~3.25 eV[44] and even higher[45]) results in negligible TPA at the excitation wavelength with the observed nonlinear absorption attributed to the 3PA process. In the presence of the GaSe layer, the power ratio shows a very different behavior with an initial decrease followed by an increase. This is attributed to saturable absorption due to the filling of defect states at low power levels followed by reverse saturable absorption due to the multiphoton absorption process at higher power levels. A similar trend has previously been reported in intensity dependent absorption measurements from stand-alone TMDC (transition-metal dichalcogenide) flakes[46] but, to the best of our knowledge, not reported in waveguide integrated 2D materials.

The TPA and 3PA coefficients can be quantitatively extracted from the power ratio plots. The evolution of the peak optical power along the waveguide in the presence of linear absorption, saturable absorption, TPA from the GaSe integrated section, and 3PA from the bare Si$_3$N$_4$ waveguide can be modeled using the following differential equation:[42,47]

$$\frac{dP}{dz} = -\left(\alpha + \frac{\Delta\alpha}{1 + \frac{P}{P_{sat}}}\right)P - \frac{\beta_{TPA-SiN-GaSe}}{a_{eff}}P^2 - \frac{\gamma_{3PA-SiN}}{a_{eff}^2}P^3, \quad (1)$$

where $P(z)$ denotes the optical power along the waveguide and α and $\Delta\alpha$ refer to the linear propagation losses from the bare Si$_3$N$_4$ waveguide and any excess propagation loss due to the transferred 2D material, respectively. $\beta_{TPA-SiN-GaSe}$ and $\gamma_{3PA-SiN}$ refer to the TPA coefficient of the waveguide with the GaSe flake on top and 3PA from the bare Si$_3$N$_4$ waveguide, respectively, with the effective modal area given as a_{eff}.

The above model ignores the effect of free-carrier absorption (FCA),[48] which is pronounced for pulsed excitation when the free-carrier lifetimes are longer than the temporal separation of the optical pulses, thereby resulting in carrier accumulation between successive pulses. Carrier lifetimes as short as 25 ps have been reported for monolayer 2D materials,[49–51] which increase to ~1 ns for multilayer 2D materials.[49] In the context of multilayer GaSe with

tens of nm thickness, the carrier lifetimes reported are in the range of 150–300 ps.[50] These numbers are much smaller in comparison with the period of the incident optical pulses (12.5 ns), thereby justifying the omission of FCA in this model and considering only multiphoton absorption processes.

The determination of TPA and 3PA coefficients for the two small GaSe flakes integrated on top of a small section of the Si$_3$N$_4$ waveguide requires Eq. (1) to be solved considering the spatial variation of optical nonlinearities for the different sections, as indicated in the lumped model shown in the inset of Fig. 1(e). For light propagation along the waveguide, we consider the linear propagation loss and 3PA in the waveguide sections without the GaSe flake ($\alpha \neq 0$, $\Delta\alpha = 0$, and $\gamma_{3PA-SiN} \neq 0$) and linear propagation losses, TPA, and 3PA in the waveguide sections with the GaSe flake ($\alpha \neq 0$, $\Delta\alpha \neq 0$, $\beta_{TPA-SiN-GaSe} \neq 0$, and $\gamma_{3PA-SiN} \neq 0$). We also consider an additional coupling loss at the beginning and end of the GaSe section of the waveguide due to possible mode mismatch. Optical nonlinearities are considered in the tapered waveguide sections but are ignored for the two grating couplers. This is due to the lower optical intensity of light incident on the gratings when compared to the straight waveguide, the short length scale of the grating section, and negligible field enhancement within the gratings due to the use of broadband, low quality factor resonant coupler design. This is further discussed in Fig. S8 of the supplementary material. We numerically solve Eq. (1) to estimate the TPA and 3PA coefficients that result in the best fit for the R vs P_{in} plot shown in Fig. 1(f). The quality of the fit for the experimental data is quantified using a mean square error (MSE) metric, defined as $\frac{1}{N}\sum_{i=1}^{N}\left(R_{expt} - R_{fit}\right)^2$, with N referring to the number of data points fitted.

For the Si$_3$N$_4$ waveguide without the GaSe layer, the 3PA coefficient for the bare Si$_3$N$_4$ waveguide is extracted as 7.876 × 10^{-6} cm^3/GW^2. The corresponding fit to the experimental data points is shown in Fig. 1(f) as the green solid curve. The 3PA coefficient for the guided-wave structure can be related to that of the bulk medium using the following overlap integral:

$$\gamma_{3PA-SiN} = \gamma_{3PA-SiN_{bulk}} \frac{\iint_{0,0}^{h,w}|E(x,y)|^2 dxdy}{\iint_{-\infty,-\infty}^{\infty,\infty}|E(x,y)|^2 dxdy}, \quad (2)$$

where $\gamma_{3PA-SiN_{bulk}}$ and $\gamma_{3PA-SiN}$ denote the 3PA coefficient of the bulk Si$_3$N$_4$ and Si$_3$N$_4$ waveguides, respectively, and h and w are the height and width of the waveguide, respectively. A similar approach has been used to calculate the refractive index change due to self-phase modulation in the context of optical fibers.[52] Considering the modal overlap with the Si$_3$N$_4$ waveguide core (80.1%), the 3PA coefficient of bulk Si$_3$N$_4$ is obtained as 9.832 × 10^{-6} cm^3/GW^2.

We also perform an analytical fit to the 3PA data in the case of the uniform cross section Si$_3$N$_4$ waveguide without the GaSe flake by solving Eq. (1) in the presence of propagation losses and 3PA coefficient terms only. The analytical solution to the above equation relating the power ratio, R, and the 3PA coefficient, $\gamma_{3PA-SiN}$, is obtained as

$$R^2 = \frac{1 + \frac{\gamma_{3PA-SiN}}{a_{eff}^2} P_{in}^2 L_{eff}^{(2)}}{\exp\left(-2\alpha L\right)}, \quad (3)$$

with $L_{eff}^{(2)}$ given as $\frac{1-\exp{(-2\alpha L)}}{\alpha}$ for a waveguide length of L. The analytical expression can be solved considering a piecewise uniform waveguide to model the tapered section. The piecewise uniform waveguide model for the tapered section and the corresponding 3PA coefficient extracted are shown in Fig. S9 of the supplementary material. We compare the numerical fit to an analytical model (black dashed curve) in Fig. 1(f), with the value of $\gamma_{3PA-SiN}$ obtained as 7.793×10^{-6} cm^3/GW^2. A very good agreement is obtained between the experimental data, numerical fit, and analytical fit, pointing to the accuracy of the parameter extraction using the numerical fitting procedure.

For the Si$_3$N$_4$ waveguides in the presence of the GaSe flake, the initial decrease in the power ratio due to saturable absorption followed by a subsequent increase due to two-photon absorption can be numerically fitted by including all the terms in Eq. (1) with the 3PA coefficient value for the bare Si$_3$N$_4$ waveguide obtained above. The best fit that minimizes the MSE is shown in Fig. 1(f) by the brown solid curve. The extracted values for $\beta_{TPA-SiN-GaSe}$, P_{sat}, $\Delta\alpha$, and coupling loss into the GaSe section are 0.117 ± 0.05 cm/GW, 95 ± 5 W, 70 ± 2 dB/mm, and 0.175 ± 0.043 dB, respectively. The uncertainties in the parameters are obtained by considering the variation in the measured optical power of ~1%. The numerical fit that minimizes the MSE is found to follow the experimental trend with very good agreement for the TPA part of the data and some deviation observed for the saturable absorption region. Nonetheless, the power evolution model shown in Eq. (1) is found to capture the essential physics of the intensity dependent transmission process. The TPA coefficient of the stand-alone GaSe flake can be obtained using the following overlap integral:

$$\beta_{TPA-SiN-GaSe} = \beta_{TPA-GaSe} \frac{\iint_{0,0}^{h',w'} |E(x,y)|^2 dxdy}{\iint_{-\infty,-\infty}^{\infty,\infty} |E(x,y)|^2 dxdy}, \quad (4)$$

where $\beta_{TPA-GaSe}$ and $\beta_{TPA-SiN-GaSe}$ denote the TPA coefficients for the bulk GaSe and GaSe-on-Si$_3$N$_4$ waveguides, respectively, and h' and w' are the height and width of the GaSe flake, respectively. The ratio of the two integrals in Eq. (4) represents the overlap factor of the optical mode with the GaSe layer, which is estimated to be ~2.32%. The TPA coefficient for the stand-alone GaSe flake is extracted to be $\beta_{TPA-GaSe} = 5.0425 \pm 0.215$ cm/GW. The value of the TPA coefficient is in very good agreement with the previous reports of TPA from a bulk GaSe crystal in the near-infrared wavelength range.[53,54]

The GaSe flake is found to exhibit a significant excess absorption loss in the shorter near-infrared wavelength range due to the presence of defect states within the bandgap. Losses of the same order of magnitude have previously been reported for multilayer MoS$_2$ on silicon waveguides.[55,56] The defect states subsequently get filled up with increasing optical intensity, resulting in the observed saturable absorption behavior.[55] The saturable absorption effect has previously been reported in few-layer GaSe[57] and multilayer TMDC[47] by performing Z-scan measurements and has also been used to demonstrate mode-locking in fiber lasers.[55,56]

B. Single-photon absorption induced resonance tuning in GaSe integrated silicon nitride ring resonator

The multilayer GaSe flake is also transferred on top of Si$_3$N$_4$ ring resonators using the procedure described in Sec. II. The optical image of the Si$_3$N$_4$ ring resonator with a ring-to-waveguide spacing and coupling length of 110 nm and 1.6 μm, respectively, is shown in Fig. 2(a). The GaSe flake on top of the ring resonator is shown in the optical image of Fig. 2(a). A zoomed-in view of a portion of the ring with the transferred GaSe flake (highlighted by the gray shaded region) is shown in Fig. 2(b) with an AFM line scan (at the location indicated by the arrow) showing a flake thickness of ~15 nm. The
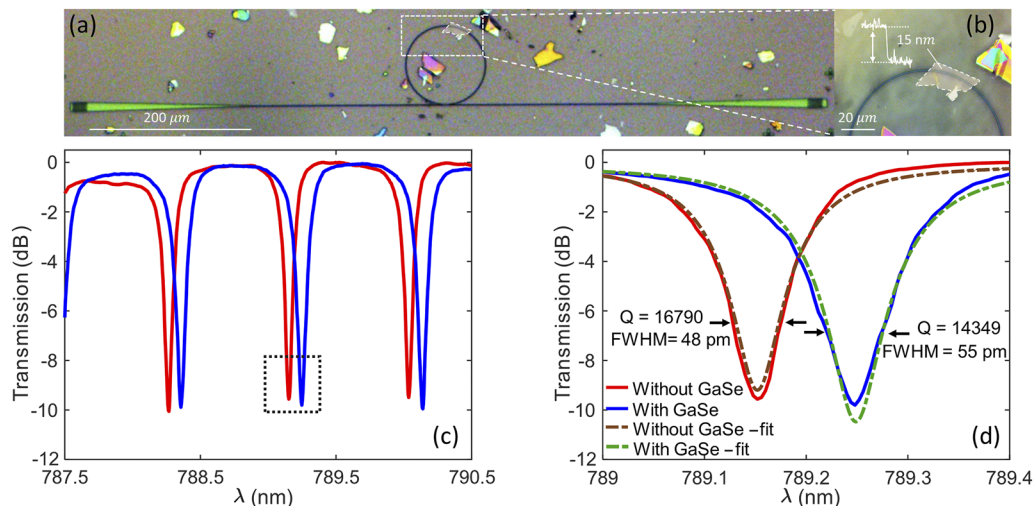

FIG. 2. (a) Optical image of the ring resonator with the GaSe flake transferred on top. (b) Zoomed-in view of the ring with the overlapping GaSe region highlighted. The AFM line scan across the region indicated by the solid line is also shown. (c) Ring resonator spectra without (red curve) and with (blue curve) the GaSe flake. (d) Zoomed-in view of one of the resonances [indicated by the dashed box in (c)] and the corresponding resonance fit shown by the dashed–dotted curves. The Q-factor and spectral width are also shown for the two resonances.

GaSe flake covers ~35.1 μm of the length of the ring resonator as measured using the optical image.

A super-luminescent diode (SLD) (QPhotonics, QSDM-780-15D) spanning 770–805 nm wavelength is used as the excitation source to measure the resonances. A polarization controller is used to maximize light coupling through the grating coupler for the straight waveguides with the same settings used for the ring resonator measurements. The resonance spectra are acquired using a fiber-coupled optical spectrum analyzer (OSA, Yokogawa, AQ6370). Figure 2(c) shows the spectra of the ring resonator without (red curve) and with (blue curve) the GaSe flake. Figure 2(d) shows a zoomed-in view of one of the resonances [denoted by the dashed box in Fig. 2(c)]. The spectral width is measured as 48 and 55 pm full width at half maximum (FWHM), with the corresponding quality factor (Q-factor) calculated as 16 790 and 14 349, respectively. The small reduction in Q-factor in the presence of the GaSe flake is attributed to the increase in linear losses.[55,56] The resonance contrast is, however, found to improve slightly in the presence of GaSe, which is attributed to the change under coupling condition in the presence of the 2D material.[55,56] The top-view optical image of the ring resonator with the light coupled from the bus waveguide is shown in Fig. S7 of the supplementary material.

For single-photon absorption studies, a continuous-wave blue laser at 450 nm is focused on the GaSe flake using a 10×/0.28 NA objective lens through the side port of the zoom lens system (No. 89-888, in-line illumination, Edmund Optics) used for visualizing the ring resonators during testing. The spot diameter of the blue laser beam is estimated to be ~2 μm on the GaSe flake. Figure 3(a) shows the resonance spectra measured for varying blue laser powers

(P_b). Figure 3(b) shows a zoomed-in view of one of the resonances [indicated by the dashed rectangle box in Fig. 3(a)]. The blue shift of the resonance wavelength is observed with increasing blue laser power. Figure 3(c) shows the plot of resonance wavelength (λ_{res}) for the chosen resonance with increasing blue laser power (data points) and the corresponding linear fit (solid lines). The resonance shift is measured both before (red data points) and after (blue data points) the transfer of the GaSe flake. The resonance wavelength shift with increasing blue laser power is estimated to be −12.3 pm/mW. For the measurements in the absence of the GaSe flake, a much smaller red shift of +0.9 pm/mW slope is observed. Figure 3(d) shows the change in Q-factor with increasing blue laser power for the chosen resonance. The Q-factor is found to exhibit a small but measurable decrease from the maximum value of 1.45×10^4–1.23×10^4 with an increase in the blue laser power. The other resonances that are measured over the SLD wavelength range also exhibit a very similar change in the resonance wavelength and Q-factor with increasing blue laser power and hence are not explicitly shown here.

The blue shift observed in the resonances with blue laser excitation is attributed to the free-carrier refraction effect due to single-photon absorption induced free carriers.[58] This results in the modulation of the refractive index within the ring segment with the GaSe flake. In the absence of the GaSe flake, a small red shift is observed in the resonances, which is attributed to the thermo-optic effect[55,56] due to local heating of the resonator. With increasing blue laser power incident on the GaSe flake, free-carrier refraction effects dominate over thermal effects, resulting in a dominant blue shift of the resonance. The single-photon absorption process also results in increased free-carrier absorption for the SLD light guided along
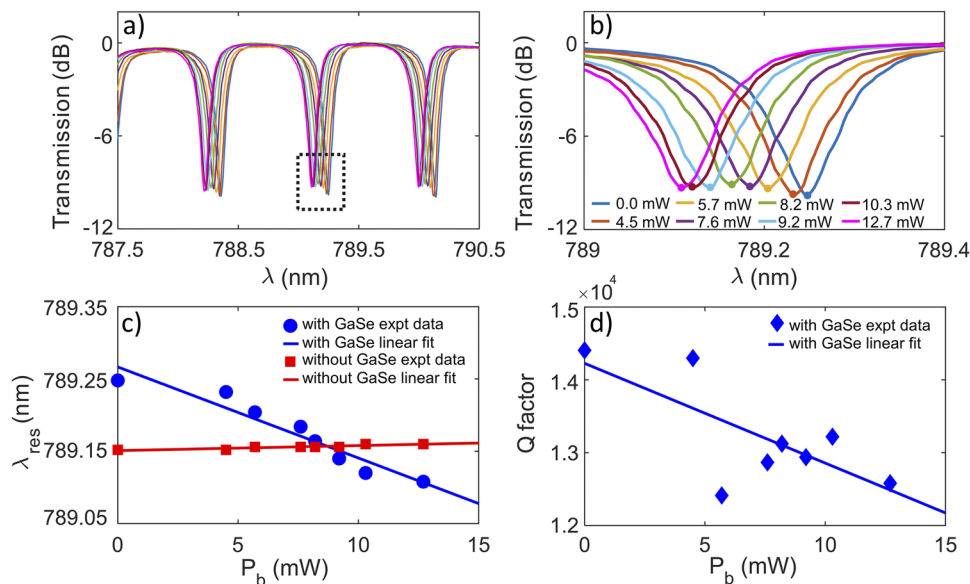

FIG. 3. (a) Si₃N₄ ring resonator resonance spectra shown as a function of varying blue laser power. (b) Zoomed-in view of one of the resonances indicated by the dashed rectangular box in (a). (c) Variation in the resonance wavelength as a function of increasing blue laser power in the presence (blue data points) and absence (red data points) of the GaSe flake on top of the ring resonator. The linear fit to the data points is shown by the solid lines. (d) Variation in the extracted Q-factor of the resonances as a function of increasing blue laser power. The linear fit to the data points is also shown.

07 November 2023 04:27:21

the ring resonator. This blue laser power dependent absorption process leads to resonance broadening and an overall reduction in the Q-factor of the resonances.

We extract the free-carrier induced refractive index and absorption change as a function of the blue laser power. A schematic of the ring resonator with a GaSe flake and incident blue laser is shown in Fig. 4(a). We consider the ring resonator to be divided into three segments, with segments 1 and 3 without the GaSe flake (lengths L_1 and L_3) with identical effective indices $\left(n_{eff1} = n_{eff3}\right)$ and absorption coefficients $(\alpha_1 = \alpha_3)$. Segment 2 of length L_2 with the GaSe flake on top is considered to have a modified effective index $\left(n_{eff2} = n_{eff2-o} + \Delta n_{FC}\right)$ and an absorption coefficient $(\alpha_2 = \alpha_{2-o} + \Delta\alpha_{FC})$. Δn_{FC} and $\Delta\alpha_{FC}$ refer to the free carrier induced change in the refractive index and absorption coefficient, respectively, in segment 2. The transmission characteristic of the ring resonator is given as[59]

$$T = \frac{a^2 + r^2 - 2ar\cos\phi}{1 + a^2 r^2 - 2ar\cos\phi}, \tag{5}$$

where a and r refer to the loss factor and self-coupling coefficient, respectively. The total phase shift, ϕ, and total loss factor, a, are defined as

$$\phi = \phi_1 + \phi_2 + \phi_3, \tag{6}$$

$$a = a_1 a_2 a_3, \tag{7}$$

where the phase shifts for the individual section are given as $\phi_i = \frac{2\pi n_{effi}}{\lambda_{res}}L_i$ and the loss factor for the individual section written as a function of propagation loss is $a_i^2 = e^{-\alpha_i L_i}$.

From the optical image of the GaSe flake of the integrated Si_3N_4 ring resonator shown in Fig. 2(a), we extract $L_1 = 140\ \mu m$, $L_2 = 35.1\ \mu m$, and $L_3 = 141.8\ \mu m$. Figure 2(d) shows the theoretical fit (dashed–dotted curves) to the experimentally measured resonances with good fit obtained for (r, a) of (0.877, 0.784) and (0.846, 0.762) in the absence and presence of GaSe, respectively. The decrease in the self-coupling coefficient is observed in the presence of the GaSe flake, which is attributed to the modification in the waveguide-to-ring coupler during the dry transfer process. The decrease in the loss factor is used to extract the excess loss in the presence of the GaSe flake, which is ~0.247 dB. It is pointed out that the excess loss in the presence of the GaSe flake for the straight waveguide (~1.2 dB) is higher than that for the ring resonator for similar coverage length and thickness. This is attributed to possible differences in the adhesion of the flake to the two devices during the dry transfer process, resulting in a reduced interaction of the optical mode with the GaSe flake for the ring resonator and increased on-resonance optical power within the ring, resulting in a small reduction in linear losses due to saturable absorption. Figure 4(b) shows the theoretical fit (solid curves) to the measured resonance spectra for two different blue laser powers, which is used to extract the effective refractive index and absorption within the ring. Figures 4(c) and 4(d) show the change in the effective index and absorption coefficient for all the ranges of incident blue laser powers considered. With increasing blue laser power, the effective refractive index of the ring 2D material section decreases due to single-photon absorption induced free-carrier refraction, which results in the observed blue shift of the resonance.[58] The absorption coefficient obtained for the ring 2D material section increases due to associated free-carrier absorption.
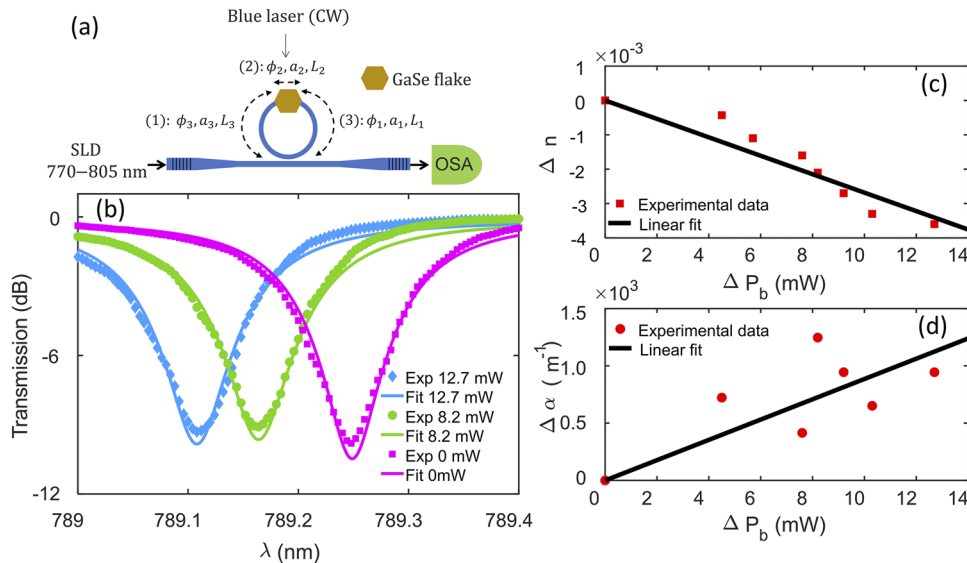
FIG. 4. (a) Schematic of the Si_3N_4 ring resonator with the GaSe flake integrated showing the three different segments along the ring. (b) The measured resonance spectra (data points) and theoretical fit (solid curves) for an incident blue laser power of 0 mW (pink curve), 8.2 mW (green curve), and 12.7 mW (blue curve). (c) Extracted effective refractive index change as a function of increasing blue laser power. (d) Extracted absorption coefficient change as a function of increasing blue laser power. The black lines shown in (c) and (d) are the linear fits to the data points.

C. Two-photon absorption induced resonance tuning in GaSe integrated silicon nitride ring resonator

For the multiphoton absorption experiments, we use a Si_3N_4 ring resonator with a ring-to-waveguide spacing of 115 nm, a coupling length of 1.6 μm, and an ~14 nm thick GaSe flake dry-transferred on top of the ring. The optical image of the ring and a zoomed-in view of the region with three small GaSe flakes on top are shown in Figs. 5(a) and 5(b), respectively. The AFM image indicating the thickness of the GaSe flake is shown as an inset in Fig. 5(b). The freshly exfoliated GaSe flake is transferred on top of the ring resonator for these experiments rather than using the same devices as in Sec. III B to ensure that the optical properties of the GaSe are not modified due to continuous ambient exposure.[60] The GaSe flake is found to break down into three smaller sections during the dry transfer process as shown in the optical image of Fig. 5(b). This can result in increased coupling losses but still exhibit resonance tuning due to multiphoton absorption. The pulsed light source used for the two-photon absorption studies discussed in Sec. III A is used here as the excitation source to measure the resonance spectra at varying input power levels. The excitation pulse width used here is shorter than the cavity round trip time. The out-coupled light is expected to show cavity ring down-like temporal characteristics with an exponential decay of the train of pulses. The Fourier transform of such a pulse train still shows resonance features in the spectral domain similar to the continuous wave or long pulse excitation.[61] The

resonance spectra and their power dependence measured using an OSA are shown in Fig. 5(c). The measured resonance spectra show clear resonance characteristics from the ring resonator with a prominent oscillatory background due to the multiple spectral modes of the pulsed excitation source used. The comparison of the incident pulsed laser source and the ring resonator spectra is shown in Fig. S9 of the supplementary material. At low incident power levels, the Q-factors extracted from the resonance profiles are in the range of 8.5×10^3–1.5×10^4, which are comparable to the measurements shown in Fig. 2 under SLD excitation. This shows that the inherent oscillatory behavior of the pulsed excitation source has a negligible effect on the measured ring resonator resonances.

A zoomed-in view of one of the resonances denoted by the dashed rectangular box is shown in Fig. 5(d). The change in the resonance wavelength with increasing power is shown in Fig. 5(e) both in the absence and in the presence of GaSe flake on top of the ring resonator. In the absence of the GaSe flake, a red shift in the resonance wavelength with a slope of 0.141 pm/mW is observed. The small red shift is attributed to the thermo-optic effect[62] from the pulsed input excitation, similar to the single-photon absorption case shown in Fig. 3(c). In the presence of the GaSe flake, a slight red shift comparable to the above case followed by a strong blue shift of the resonances is observed. The slope of the observed blue shift is estimated to be −0.4755 pm/mW. This blue shift of the resonances is attributed to the two-photon absorption induced free-carrier refraction effect
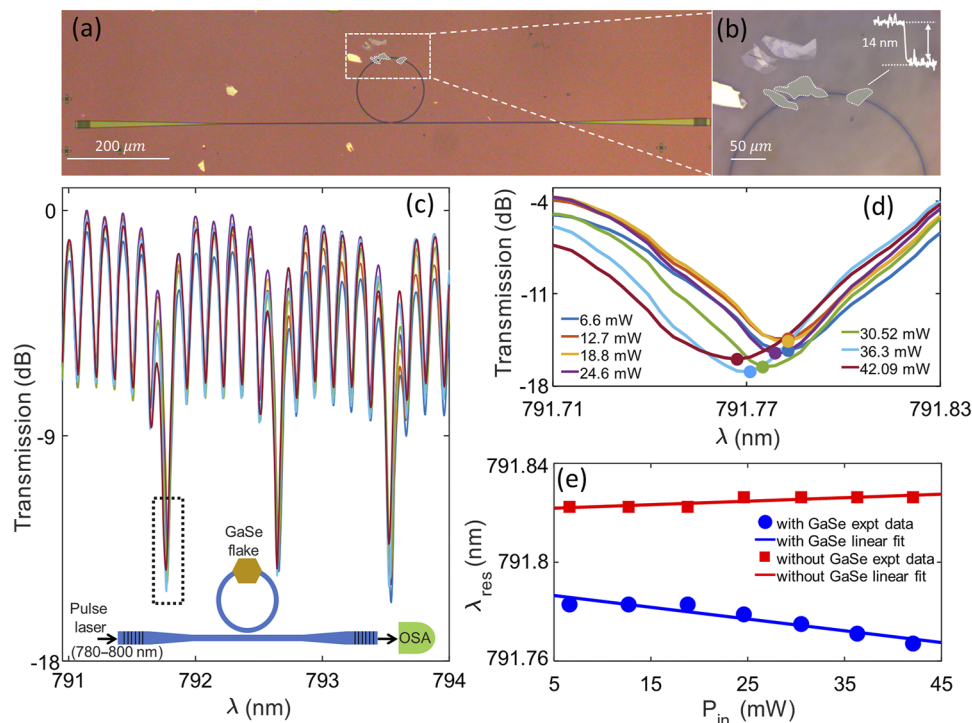

FIG. 5. (a) Optical image of the ring resonator with GaSe transferred on top. (b) Zoomed-in view of the ring with the overlapping GaSe region highlighted. (c) Ring resonator resonance spectra shown as a function of varying input power. (d) Close-up view of one of the resonances. (e) Change in the resonance wavelength as a function of varying input power with (blue data points) and without (red data points) GaSe on the ring. The solid lines indicate the linear fit to the data.

resulting in the modulation of the refractive index within the ring structure.[58] As expected, the blue shift of the resonances due to two-photon absorption is smaller in comparison with the single-photon absorption studies discussed previously. The measured resonance spectra exhibit spectral shifts and do not show any spectral distortion or bistability with increasing two-photon absorption strength.[63] This points to the nonlinear absorption process being significant to cause the spectral shift but still weak enough to not result in spectral distortion or hysteresis over the range of incident optical powers used in this study.

IV. CONCLUSIONS

In this work, we have presented single- and multiphoton absorption studies in multilayer GaSe integrated Si_3N_4 waveguides and ring resonator structures. GaSe is a promising layered material with strong optical nonlinearities, making it attractive for realizing active optical functionalities when integrated with a Si_3N_4 integrated photon platform in the shorter near-infrared wavelength range. A straight waveguide integrated with multilayer GaSe exhibits saturable absorption at low power levels followed by two-photon absorption at higher power levels. A TPA coefficient of 0.117 cm/GW for the GaSe–Si_3N_4 composite waveguide and a 3PA coefficient of 7.876×10^{-6} cm^3/GW^2 for the bare Si_3N_4 waveguide are obtained from intensity dependent transmission measurements. The multiphoton absorption process in such hybrid waveguide structures can find potential applications as on-chip saturable absorbers, optical power limiters,[64] and multiphoton detectors.[65] Ring resonators integrated with multilayer GaSe are used to demonstrate single- and multiphoton absorption induced resonance tuning. Single-photon absorption induced resonance tuning is achieved using a blue laser incident on top of GaSe to include free-carrier generation using the band-to-band absorption. Free-carrier refraction and absorption effects result in a strong blue shift of the resonance and a reduction in the Q-factor as a function of increasing blue laser power. The two-photon absorption induced resonance tuning is achieved using a near-infrared pulsed laser coupled to the Si_3N_4 waveguide. The resonance tuning mechanisms studied here are particularly promising for realizing all-optical control of light for optical modulation and switching applications.[66] The present study is aimed at studying the effect of single- and two-photon absorption induced modulation of optical properties in Si_3N_4 integrated photonic devices in the presence of 2D materials. A further improvement to the optical losses[67] and Q-factor of the resonant structures[68] is expected to boost the overall efficiency of all-optical control in such devices, which would be useful for transitioning from these proof-of-concept demonstrations to useful device applications.

SUPPLEMENTARY MATERIAL

See the supplementary material for the details on the following: the SEM image of the waveguide with multilayer GaSe on top, Raman spectra, and second and third harmonic generation images of the GaSe flake on top of the Si_3N_4 waveguide; the cut-back measurements of the Si_3N_4 waveguide with and without the GaSe flake; the measured optical spectra at the input and output of the waveguide with and without the GaSe flake; the simulated dispersion profile of the Si_3N_4 waveguide with and without GaSe on top; the optical image of light coupling into the Si_3N_4 waveguide and ring resonator; the simulated electric field of the light coupled into the waveguide through the grating coupler, estimate of the optical intensity of the light incident on the grating coupler and waveguide section; the piecewise uniform waveguide model for the tapered section and its effect on the extracted 3PA coefficient from the Si_3N_4 waveguide and measured optical spectra for the pulsed laser source used in the two-photon absorption studies; and the measured optical spectra of the pulsed excitation and the ring resonator resonances.

AUTHOR DECLARATIONS

Conflict of Interest

The authors have no conflicts to disclose.

Author Contributions

Asish Prosad: Formal analysis (equal); Investigation (lead); Methodology (lead); Writing – original draft (lead). **Rabindra Biswas**: Investigation (supporting); Methodology (supporting); Writing – review & editing (supporting). **Lal Krishna A S**: Methodology (supporting); Writing – review & editing (supporting). **T. Srinivas**: Writing – review & editing (supporting). **Varun Raghunathan**: Conceptualization (lead); Formal analysis (supporting); Funding acquisition (lead); Project administration (lead); Writing – review & editing (lead).

DATA AVAILABILITY

The data that support the findings of this study are available from the corresponding author upon reasonable request.

REFERENCES

[1]R. S. El Shamy, M. A. Swillam, and X. Li, "Optimization of silicon nitride waveguide platform for on-chip virus detection," Sensors **22**, 1152 (2022).
[2]G. Pezzotti, "Silicon nitride: A bioceramic with a gift," ACS Appl. Mater. Interfaces **11**, 26619–26636 (2019).
[3]C. Taballione, R. van der Meer, H. J. Snijders, P. Hooijschuur, J. P. Epping, M. de Goede, B. Kassenberg, P. Venderbosch, C. Toebes, H. van den Vlekkert, P. W. H. Pinkse, and J. J. Renema, "A universal fully reconfigurable 12-mode quantum photonic processor," Mater. Quantum Technol. **1**, 035002 (2021).
[4]J. M. Chavez Boggio, D. Bodenmüller, T. Fremberg, R. Haynes, M. M. Roth, R. Eisermann, M. Lisker, L. Zimmermann, and M. Böhm, "Dispersion engineered

silicon nitride waveguides by geometrical and refractive-index optimization," J. Opt. Soc. Am. B **31**, 2846 (2014).

[5] A. Prokhodtsov, V. Kovalyuk, P. An, A. Golikov, R. Shakhovoy, V. Sharoglazova, A. Udaltsov, Y. Kurochkin, and G. Goltsman, "Silicon nitride Mach-Zehnder interferometer for on-chip quantum random number generation," J. Phys.: Conf. Ser. **1695**, 012218 (2020).

[6] D. J. Moss, R. Morandotti, A. L. Gaeta, and M. Lipson, "New CMOS-compatible platforms based on silicon nitride and Hydex for nonlinear optics," Nat. Photonics **7**, 597–607 (2013).

[7] M. A. G. Porcel, F. Schepers, J. P. Epping, T. Hellwig, M. Hoekman, R. G. Heideman, P. J. M. van der Slot, C. J. Lee, R. Schmidt, R. Bratschitsch, C. Fallnich, and K.-J. Boller, "Two-octave spanning supercontinuum generation in stoichiometric silicon nitride waveguides pumped at telecom wavelengths," Opt. Express **25**, 1542 (2017).

[8] C. J. Krückel, V. Torres-Company, P. A. Andrekson, D. T. Spencer, J. F. Bauters, M. J. R. Heck, and J. E. Bowers, "Continuous wave-pumped wavelength conversion in low-loss silicon nitride waveguides," Opt. Lett. **40**, 875 (2015).

[9] N. M. Lupken, T. Wurthwein, K. J. Boller, and C. Fallnich, "Optical parametric amplification in silicon nitride waveguides for coherent Raman imaging," in *2021 Conference on Lasers and Electro-Optics, CLEO 2021 - Proceedings* (Institute of Electrical and Electronics Engineers, Inc., 2021), Vol. 7, pp. 10424–10453.

[10] H. Guo, C. Herkommer, A. Billat, D. Grassani, C. Zhang, M. H. P. Pfeiffer, W. Weng, C. S. Brès, and T. J. Kippenberg, "Mid-infrared frequency comb via coherent dispersive wave generation in silicon nitride nanophotonic waveguides," Nat. Photonics **12**, 330–335 (2018).

[11] A. W. Elshaari, I. E. Zadeh, K. D. Jöns, and V. Zwiller, "Thermo-optic characterization of silicon nitride resonators for cryogenic photonic circuits," IEEE Photonics J. **8**, 2701009 (2016).

[12] W. Jin, R. G. Polcawich, P. A. Morton, and J. E. Bowers, "Phase tuning by length contraction," Opt. Express **26**, 3174 (2018).

[13] C. Op de Beeck, B. Haq, L. Elsinger, A. Gocalinska, E. Pelucchi, B. Corbett, G. Roelkens, and B. Kuyken, "Heterogeneous III-V on silicon nitride amplifiers and lasers via microtransfer printing," Optica **7**, 386 (2020).

[14] S. Cuyvers, A. Hermans, M. Kiewiet, J. Goyvaerts, G. Roelkens, K. van Gasse, D. van Thourhout, and B. Kuyken, "Heterogeneous integration of Si photodiodes on silicon nitride for near-visible light detection," Opt. Lett. **47**, 937 (2022).

[15] L. Chang, M. H. P. Pfeiffer, N. Volet, M. Zervas, J. D. Peters, C. L. Manganelli, E. J. Stanton, Y. Li, T. J. Kippenberg, and J. E. Bowers, "Heterogeneous integration of lithium niobate and silicon nitride waveguides for wafer-scale photonic integrated circuits on silicon," Opt. Lett. **42**, 803 (2017).

[16] J. Susoma, L. Karvonen, A. Säynätjoki, S. Mehravar, R. A. Norwood, N. Peyghambarian, K. Kieu, H. Lipsanen, and J. Riikonen, "Second and third harmonic generation in few-layer gallium telluride characterized by multiphoton microscopy," Appl. Phys. Lett. **108**(7), 073103 (2016).

[17] A. Säynätjoki, L. Karvonen, H. Rostami, A. Autere, S. Mehravar, A. Lombardo, R. A. Norwood, T. Hasan, N. Peyghambarian, H. Lipsanen, K. Kieu, A. C. Ferrari, M. Polini, and Z. Sun, "Ultra-strong nonlinear optical processes and trigonal warping in MoS_2 layers," Nat. Commun. **8**, 893 (2017).

[18] A. Autere, H. Jussila, Y. Dai, Y. Wang, H. Lipsanen, and Z. Sun, "Nonlinear optics with 2D layered materials," Adv. Mater. **30**, 1705963 (2018).

[19] K. Kinoshita, R. Moriya, M. Onodera, Y. Wakafuji, S. Masubuchi, K. Watanabe, T. Taniguchi, and T. Machida, "Dry release transfer of graphene and few-layer h-BN by utilizing thermoplasticity of polypropylene carbonate," npj 2D Mater. Appl. **3**, 22 (2019).

[20] T. F. Schranghamer, M. Sharma, R. Singh, and S. Das, "Review and comparison of layer transfer methods for two-dimensional materials for emerging applications," Chem. Soc. Rev. **50**, 11032–11054 (2021).

[21] D. H. Lee, Y. Sim, J. Wang, and S. Y. Kwon, "Metal-organic chemical vapor deposition of 2D van der Waals materials—The challenges and the extensive future opportunities," APL Mater. **8**, 030901 (2020).

[22] L. Tang, J. Tan, H. Nong, B. Liu, and H. M. Cheng, "Chemical vapor deposition growth of two-dimensional compound materials: Controllability, material quality, and growth mechanism," Acc. Mater. Res. **2**, 36–47 (2021).

[23] Y. Yang, J. Wu, X. Xu, Y. Liang, S. T. Chu, B. E. Little, R. Morandotti, B. Jia, and D. J. Moss, "Invited Article: Enhanced four-wave mixing in waveguides integrated with graphene oxide," APL Photonics **3**, 120803 (2018).

[24] J. Wu, Y. Yang, X. Xu, Y. Qu, L. Jia, Y. Zhang, Y. Liang, S. T. Chu, B. E. Little, R. Morandotti, B. Jia, and D. Moss, "Graphene oxide for enhanced nonlinear optics in integrated waveguides," in OSA Advanced Photonics Congress (AP), 2019.

[25] Y. Zhang, J. Wu, Y. Yang, Y. Qu, H. El Dirani, R. Crochemore, C. Sciancalepore, P. Demongodin, C. Grillet, C. Monat, B. Jia, and D. J. Moss, "Enhanced self-phase modulation in silicon nitride waveguides integrated with 2D graphene oxide films," IEEE J. Sel. Top. Quantum Electron. **29**, 5100413 (2022).

[26] Y. Zhang, J. Wu, L. Jia, Y. Qu, Y. Yang, B. Jia, and D. J. Moss, "Graphene oxide for nonlinear integrated photonics," Laser Photonics Rev. **17**(3), 2200512 (2023).

[27] Y. Zhang, J. Wu, Y. Yang, Y. Qu, L. Jia, H. E. Dirani, S. Kerdiles, C. Sciancalepore, P. Demongodin, C. Grillet, C. Monat, B. Jia, and D. J. Moss, "Enhanced supercontinuum generation in integrated waveguides incorporated with graphene oxide films," Adv. Mater. Technol. **8**(9), 2201796 (2023).

[28] Q. Feng, H. Cong, B. Zhang, W. Wei, Y. Liang, S. Fang, T. Wang, and J. Zhang, "Enhanced optical Kerr nonlinearity of graphene/Si hybrid waveguide," Appl. Phys. Lett. **114**, 071104 (2019).

[29] P. Demongodin, H. El Dirani, S. Kerdilès, J. Lhuillier, T. Wood, C. Sciancalepore, and C. Monat, "Pulsed four-wave mixing at telecom wavelengths in Si_3N_4 waveguides locally covered by graphene," Nanomaterials **13**(3), 451 (2023).

[30] L. Liu, K. Xu, X. Wan, J. Xu, C. Y. Wong, and H. K. Tsang, "Enhanced optical Kerr nonlinearity of MoS_2 on silicon waveguides," Photonics Res. **3**(5), 206 (2015).

[31] Y. Wang, Z. Yu, Z. Zhang, B. Sun, Y. Tong, J. B. Xu, X. Sun, and H. K. Tsang, "Bound-states-in-continuum hybrid integration of 2D platinum diselenide on silicon nitride for high-speed photodetectors," ACS Photonics **7**(10), 2643–2649 (2020).

[32] Y. Zhang, L. Tao, D. Yi, J. B. Xu, and H. K. Tsang, "Enhanced thermo-optic nonlinearities in a MoS_2-on-silicon microring resonator," Appl. Phys. Express **13**, 022004 (2020).

[33] Y. Zhang, L. Tao, D. Yi, J. B. Xu, and H. K. Tsang, "Enhanced four-wave mixing with MoS_2 on a silicon waveguide," J. Opt. **22**, 025503 (2020).

[34] Y. Wang, V. Pelgrin, S. Gyger, G. M. Uddin, X. Bai, C. Lafforgue, L. Vivien, K. D. Jöns, E. Cassan, and Z. Sun, "Enhancing Si_3N_4 waveguide nonlinearity with heterogeneous integration of few-layer WS_2," ACS Photonics **8**, 2713–2721 (2021).

[35] S. Deckoff-Jones, V. Pelgrin, J. Zhang, C. Lafforgue, L. Deniel, S. Guerber, R. Ribeiro-Palau, F. Boeuf, C. Alonso-Ramos, L. Vivien, J. Hu, and S. Serna, "Enhancing SiN waveguide optical nonlinearity via hybrid GaS integration," J. Opt. **23**, 025802 (2021).

[36] Z. Zhao, Z. Zhang, J. Li, Z. Shang, G. Wang, J. Yin, H. Chen, K. Guo, and P. Yan, "MoS_2 hybrid integrated micro-ring resonator phase shifter based on a silicon nitride platform," Opt. Lett. **47**, 949 (2022).

[37] X. Li, M. W. Lin, J. Lin, B. Huang, A. A. Puretzky, C. Ma, K. Wang, W. Zhou, S. T. Antelides, M. Hi, I. Kravchenko, J. Fowlkes, C. M. Ouleau, D. B. Geohegan, and K. Xiao, "Two-dimensional GaSe/$MoSe_2$ misfit bilayer heterojunctions by van der Waals epitaxy," Sci. Adv **2**, e1501882 (2016).

[38] L. Karvonen, A. Säynätjoki, S. Mehravar, R. D. Rodriguez, S. Hartmann, D. R. T. Zahn, S. Honkanen, R. A. Norwood, N. Peyghambarian, K. Kieu, H. Lipsanen, and J. Riikonen, "Investigation of second- and third-harmonic generation in few-layer gallium selenide by multiphoton microscopy," Sci. Rep. **5**, 10334 (2015).

[39] W. Jie, X. Chen, D. Li, L. Xie, Y. Y. Hui, S. P. Lau, X. Cui, and J. Hao, "Layer-dependent nonlinear optical properties and stability of non-centrosymmetric modification in few-layer GaSe sheets," Angew. Chem., Int. Ed. **54**, 1185–1189 (2015).

[40] P. Gant, F. Carrascoso, Q. Zhao, Y. K. Ryu, M. Seitz, F. Prins, R. Frisenda, and A. Castellanos-Gomez, "A system for the deterministic transfer of 2D materials under inert environmental conditions," 2D Mater. **7**, 025034 (2020).

[41] See https://www.lumerical.com/products/fdtd/ for Lumerical FDTD.

[42] R. Claps, D. Dimitropoulos, V. Raghunathan, Y. Han, and B. Jalali, "Observation of stimulated Raman amplification in silicon waveguides," Opt. Express **11**(15), 1731–1739 (2003).

[43] R. W. Boyd, *Nonlinear Optics* (Academic Press, 2020).

[44] C. J. Krückel, A. Fülöp, Z. Ye, P. A. Andrekson, and V. Torres-Company, "Optical bandgap engineering in nonlinear silicon nitride waveguides," Opt. Express **25**, 15370 (2017).

[45]K. J. A. Ooi, D. K. T. Ng, T. Wang, A. K. L. Chee, S. K. Ng, Q. Wang, L. K. Ang, A. M. Agarwal, L. C. Kimerling, and D. T. H. Tan, "Pushing the limits of CMOS optical parametric amplifiers with USRN:Si$_7$N$_3$ above the two-photon absorption edge," Nat. Commun. **8**, 13878 (2017).

[46]N. Dong, Y. Li, S. Zhang, N. McEvoy, R. Gatensby, G. S. Duesberg, and J. Wang, "Saturation of two-photon absorption in layered transition metal dichalcogenides: Experiment and theory," ACS Photonics **5**, 1558–1565 (2018).

[47]S. Zhang, N. Dong, N. McEvoy, M. OBrien, S. Winters, N. C. Berner, C. Yim, Y. Li, X. Zhang, Z. Chen, L. Zhang, G. S. Duesberg, and J. Wang, "Direct observation of degenerate two-photon absorption and its saturation in WS$_2$ and MoS$_2$ monolayer and few-layer films," ACS Nano **9**, 7142–7150 (2015).

[48]A. Rahim, E. Ryckeboer, A. Z. Subramanian, S. Clemmen, B. Kuyken, A. Dhakal, A. Raza, A. Hermans, M. Muneeb, S. Dhoore, Y. Li, U. Dave, P. Bienstman, N. Le Thomas, G. Roelkens, D. van Thourhout, P. Helin, S. Severi, X. Rottenberg, and R. Baets, "Expanding the silicon photonics portfolio with silicon nitride photonic integrated circuits," J. Lightwave Technol. **35**, 639–649 (2017).

[49]H. Wang, C. Zhang, and F. Rana, "Surface recombination limited lifetimes of photoexcited carriers in few-layer transition metal dichalcogenide MoS$_2$," Nano Lett. **15**, 8204–8210 (2015).

[50]X. Zhang, S. Wang, G. Wan, Y. Zhang, M. Huang, and L. Yi, "Transient reflectivity measurement of photocarrier dynamics in GaSe thin films," Appl. Phys. B **123**, 86–87 (2017).

[51]Y. Wang, Z. Nie, and F. Wang, "Modulation of photocarrier relaxation dynamics in two-dimensional semiconductors," Light: Sci. Appl. **9**, 192 (2020).

[52]G. P. Agrawal, *Nonlinear Fiber Optics*, 3rd ed. (Academic Press, 2001).

[53]I. B. Zotova and Y. J. Ding, "Spectral measurements of two-photon absorption coefficients for CdSe and GaSe crystals," Appl. Opt. **40**, 6654–6658 (2001).

[54]K. L. Vodopyanov, S. B. Mirov, V. G. Voevodin, and P. G. Schunemann, "Two-photon absorption in GaSe and CdGeAs$_2$," Opt. Commun. **155**, 47–50 (1998).

[55]G. Wei, T. K. Stanev, D. A. Czaplewski, I. W. Jung, and N. P. Stern, "Silicon-nitride photonic circuits interfaced with monolayer MoS$_2$," Appl. Phys. Lett. **107**, 091112 (2015).

[56]R. Maiti, C. Patil, R. A. Hemnani, M. Miscuglio, M. Amin, Z. Ma, R. Chaudhary, A. T. C. Johnson, L. Bartels, R. Agarwal, and V. J. Sorger, "Loss and coupling tuning via heterogeneous integration of MoS$_2$ layers in silicon photonics [Invited]," Opt. Mater. Express **9**, 751 (2019).

[57]B. Shi, G. He, K. Yang, B. Zhang, and J. He, "Few-layer GaSe nanosheet-based broadband saturable absorber for passively Q-switched solid-state bulk lasers," Appl. Opt. **59**(28), 8834 (2020).

[58]Y. Gao, W. Zhou, X. Sun, H. K. Tsang, and C. Shu, "Cavity-enhanced thermo-optic bistability and hysteresis in a graphene-on-Si$_3$N$_4$ ring resonator," Opt. Lett. **42**, 1950 (2017).

[59]W. Bogaerts, P. de Heyn, T. van Vaerenbergh, K. de Vos, S. Kumar Selvaraja, T. Claes, P. Dumon, P. Bienstman, D. van Thourhout, and R. Baets, "Silicon microring resonators," Laser Photonics Rev. **6**, 47–73 (2012).

[60]Q. Zhao, R. Frisenda, P. Gant, D. Perez de Lara, C. Munuera, M. Garcia Hernandez, Y. Niu, T. Wang, W. Jie, and A. Castellanos Gomez, "Toward air stability of thin GaSe devices: Avoiding environmental and laser induced degradation by encapsulation," Adv. Funct. Mater. **28**, 1805304 (2018).

[61]A. Driessen, D. H. Geuzebroek, E. J. Klein, R. Dekker, R. Stoffer, and C. Bornholdt, "Propagation of short lightpulses in microring resonators: Ballistic transport versus interference in the frequency domain," Opt. Commun. **270**, 217–224 (2007).

[62]L.-W. Luo, G. S. Wiederhecker, K. Preston, and M. Lipson, "Power insensitive silicon microring resonators," Opt. Lett. **37**, 590–592 (2012).

[63]Q. Xu and M. Lipson, "Carrier-induced optical bistability in silicon ring resonators," Opt. Lett. **31**, 341–343 (2006).

[64]J. Parra, J. Navarro-Arenas, M. Menghini, M. Recaman, J. Pierre-Locquet, and P. Sanchis, "Low-threshold power and tunable integrated optical limiter based on an ultracompact VO$_2$/Si waveguide," APL Photonics **6**, 121301 (2021).

[65]J. Li, C. Liu, H. Chen, J. Guo, M. Zhang, and D. Dai, "Hybrid silicon photonic devices with two-dimensional materials," Nanophotonics **9**, 2295 (2020).

[66]S. Yu, X. Wu, Y. Wang, X. Guo, and L. Tong, "2D materials for optical modulation: Challenges and opportunities," Adv. Mater. **29**, 1606128 (2017).

[67]M. H. P. Pfeiffer, C. Herkommer, J. Liu, T. Morais, M. Zervas, M. Geiselmann, and T. J. Kippenberg, "Photonic damascene process for low-loss, high-confinement silicon nitride waveguides," IEEE J. Sel. Top. Quantum Electron. **24**, 6101411 (2018).

[68]V. K. Surana, N. Bhardwaj, A. Rawat, Y. Yadav, S. Ganguly, and D. Saha, "Realization of high-quality silicon nitride deposition at low temperatures," J. Appl. Phys. **126**, 115302 (2019).